

Quantum spiral spin-tensor magnetism

Xiaofan Zhou,^{1,2} Xi-Wang Luo,¹ Gang Chen,^{2,3,4,*} Suotang Jia,^{2,3} and Chuanwei Zhang^{1,†}

¹*Department of Physics, The University of Texas at Dallas, Richardson, Texas 75080, USA*

²*State Key Laboratory of Quantum Optics and Quantum Optics Devices, Institute of Laser Spectroscopy, Shanxi University, Taiyuan 030006, China*

³*Collaborative Innovation Center of Extreme Optics, Shanxi University, Taiyuan, Shanxi 030006, China*

⁴*Collaborative Innovation Center of Light Manipulations and Applications, Shandong Normal University, Jinan 250358, China*

The characterization of quantum magnetism in a large spin (≥ 1) system naturally involves both spin-vectors and -tensors. While certain types of spin-vector (e.g., ferromagnetic, spiral) and spin-tensor (e.g., nematic in frustrated lattices) orders have been investigated separately, the coexistence and correlation between them have not been well explored. Here we propose a novel quantum spiral spin-tensor order on a spin-1 Heisenberg chain subject to a spiral spin-tensor Zeeman field, which can be experimentally realized using a Raman-dressed cold atom optical lattice. We develop a method to fully characterize quantum phases of such spiral tensor magnetism with the coexistence of spin-vector and spin-tensor orders as well as their correlations using eight geometric parameters. Our method provides a powerful tool for characterizing spin-1 quantum magnetism and opens an avenue for exploring novel magnetic orders and spin-tensor electronics/atomtronics in large-spin systems.

Introduction.— Quantum magnetism originates from the exchange coupling between quantum spins and lies at the heart of many fundamental phenomena in quantum physics^{1–3}. In particular, understanding exotic magnetic orders of strongly correlated quantum spin chains is one major issue of modern condensed matter physics. Such interacting many-body systems can give rise to various magnetic orders and the phase transitions between them^{4–11}. Major research efforts have been focused on spin-1/2 systems, where collinear (e.g., ferromagnetic and antiferromagnetic) and non-collinear (e.g., spiral) magnetic orders are fully characterized by the spin-vector (\vec{S}) configurations, including their local orientations and densities as well as nonlocal correlations^{12–22}.

Quantum magnetism with large spins, such as spin-1, has also received considerable attention in recent years, where the large spin could originate from, for instance, intrinsic orbital degrees of electrons or pseudo-spins defined by hyperfine states of cold neutral atoms or ions^{23–34}. Mathematically, a full description of a large spin (≥ 1) involves not only rank-1 spin-vectors, but also higher-rank spin-tensors, therefore it is expected that the resulting quantum magnetism may possess both spin-vector and tensor orders. So far, spin-vector magnetism of a strongly correlated spin-1 (or higher) chain has been extensively studied^{34–46}, and the competition between spin interaction and Zeeman field (either uniform or spiral along the chain) leads to rich phase diagrams. Certain nematic magnetic orders of spin-tensors (with vanishing spin-vector) have been investigated in 2-dimensional (D) geometrically frustrated (e.g., triangle) lattices^{47–55}. However, magnetic orders with the coexistence of these two orders have not been discovered and a unified description of such magnetic orders is still lacking. Addressing these two important issues should be of great importance for the discovery of novel magnetic orders and

the exploration of electronics/atomtronics characterized by spin-tensors.

We restrict to spin-1 magnetic orders, which may be characterized by two elements: rank-1 spin-vector (represented by an arrow using 3 parameters) and rank-2 spin-tensor (represented by an ellipsoid using 5 parameters). In this Letter, we propose a novel type of quantum spiral spin-tensor orders with the coexistence of spin-vector and tensor orders and develop a geometric method to describe them. Our main results are:

i) We propose an experimental setup for realizing a spin-1 Heisenberg chain subject to a spiral spin-tensor Zeeman field using a Raman coupled cold atom optical lattice, which can host the novel quantum spiral spin-tensor orders.

ii) We develop a method for characterizing any spin-1 quantum magnetism with the order parameters and long-range spin correlations described by eight geometric parameters originating from spin arrow and ellipsoid.

iii) We obtain the ground-state phase diagram numerically using the density-matrix renormalization group (DMRG) method and showcases its rich physics such as a ferromagnetic spiral tensor phase, where the relative orientation between spin-vector arrow and spin-tensor ellipsoid exhibits periodic oscillations. In previously studied spiral spin-vector order³⁴, arrow length, ellipsoid size, and their relative orientations are uniformly fixed across the lattice chain, while the 2D nematic phase in a frustrated lattice^{47,48} possesses vanishing spin-vector arrow and fixed ellipsoid size and directions.

The model.— We consider an experimental setup based on ultracold bosonic atoms in a 1D optical lattice, as shown in Fig. 1(a). Three Raman lasers are used to couple different spin and momentum states^{27,56–61}. In particular, a pair of counter-propagating lasers with wavelength λ_L is used to realize the 1D optical lat-

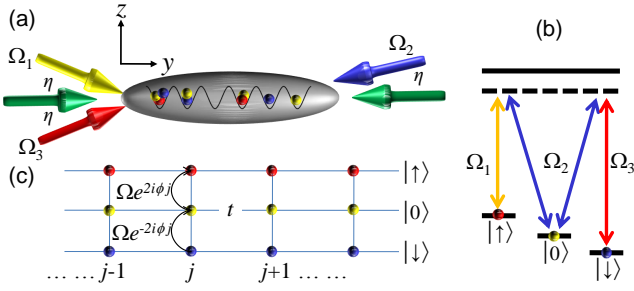


FIG. 1: (a) Schematics of the system setup. Green arrows represent the 1D optical lattice. Yellow, blue and red arrows represent three Raman lasers. (b) The Raman lasers induce two Raman transitions between spin states $|0\rangle$ and $|\uparrow(\downarrow)\rangle$. (c) Effective description of the model. t is the hopping between neighboring sites, $\Omega e^{2i\phi j} |0\rangle\langle\uparrow|$ and $\Omega e^{-2i\phi j} |\downarrow\rangle\langle 0|$ are the site-dependent couplings between different spin states.

tice $V_{\text{lat}}(y) = -V_0 \cos^2(k_L y)$ along the y -direction, with wavenumber $k_L = 2\pi/\lambda_L$. All Raman lasers have an angle η with respect to the y -direction and they induce two Raman transitions between the spin states $|0\rangle$ and $|\uparrow(\downarrow)\rangle$ [as shown in Fig. 1(b)] with the momentum transfer $2k_R$, where $k_R = 2\pi \cos(\eta)/\lambda_\Omega$ with λ_Ω the Raman-laser wavelength. Such Raman laser setup induces the spin-tensor-momentum coupling⁶¹ for ultra-cold atomic gases, which has been realized in experiment recently⁶².

The tight-binding Hamiltonian without Raman lasers can be written as $H_0 = -t \sum_{\langle i,j \rangle, \sigma} b_{i\sigma}^\dagger b_{j\sigma} + (U_0/2) \sum_j n_j (n_j - 1) + (U_2/2) \sum_j (\mathbf{S}_j^2 - 2n_j)$, where $b_{j\sigma}^\dagger$ ($b_{j\sigma}$) is the creation (annihilation) operator with a spin σ , $n_j = \sum_\sigma b_{j\sigma}^\dagger b_{j\sigma}$ is the density operator, and $\mathbf{S}_j = \sum_{\sigma\sigma'} b_{j\sigma}^\dagger \mathbf{F}_{\sigma\sigma'} b_{j\sigma}$ with $\mathbf{F}_{\sigma\sigma'}$ represent the total angular momentum $F = 1$ spin operators and $\sigma = (\uparrow, 0, \downarrow)$. t is the tunneling amplitude between neighboring sites, and U_0 and U_2 are on-site density and spin interaction strengths.

In the Mott limit of commensurate odd integer filling and $U_0, U_2 \gg t$, we can get the effective spin Hamiltonian (see Appendix A), $H_{\text{spin}}^0 = \sum_j J_1 \mathbf{S}_j \cdot \mathbf{S}_{j+1} + J_2 (\mathbf{S}_j \cdot \mathbf{S}_{j+1})^2$. Typically, $J_1 < 0$ for repulsive interaction, therefore we parameterize J_1 and J_2 on a unit circle with $J_1 = \cos \theta$ and $J_2 = \sin \theta$ and focus on the parameter region $\theta \in [0.5\pi, 1.5\pi]$. For $J_2 > J_1$ (i.e., $0.5 \leq \theta/\pi < 1.25$), the system possesses the ferromagnetic order, which maximizes $\mathbf{S}_j \cdot \mathbf{S}_{j+1}$ but minimizes $(\mathbf{S}_j \cdot \mathbf{S}_{j+1})^2$ due to dominating negative bilinear interaction J_1 . For large negative biquadratic interaction $J_2 < J_1$ in the region ($1.25 < \theta/\pi \leq 1.5$), the ground state should maximize $(\mathbf{S}_j \cdot \mathbf{S}_{j+1})^2$ by forming spin singlet between neighboring sites, which breaks the translational symmetry, leading to the dimer phase^{23–25,63}. Typical values for alkaline atoms are $\theta/\pi = 1.26$ for ^{23}Na , 1.15π for ^7Li , 1.242 for ^{41}K , and 1.249 for ^{87}Rb ²⁷.

The Raman lasers give rise to the site-dependent

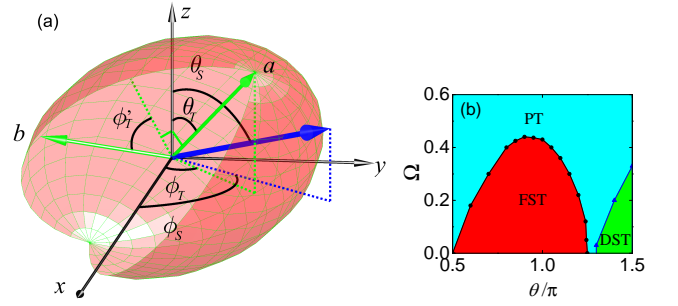


FIG. 2: (a) The description of a spin-1 magnetic order. The blue arrow denotes the spin-vector \vec{S} , in which θ_S and ϕ_S are polar angle and azimuth angle with length l_S . The red ellipsoid is the spin-tensor T , in which the green arrows are ellipsoid's orientations \vec{v}_T^n ($n = a, b$) with the principle axes lengths l_T^n . The Euler angles θ_T , ϕ_T and ϕ'_T are used to determine the orientation of ellipsoid, in which θ_T is the polar angle of \vec{v}_T^a , ϕ_T is the azimuth angle of \vec{v}_T^a , and ϕ'_T is the angle between \vec{v}_T^b and the plane formed by z -axis and \vec{v}_T^a . (b) The phase diagram of the Hamiltonian (1) with respect to (θ, Ω) for $\phi/\pi = 1/6$, which includes paramagnetic tensor (PT), ferromagnetic spiral tensor (FST) and dimer spiral tensor (DST) phases.

spin flipping terms $\Omega e^{2i\phi j} |0\rangle\langle\uparrow|$ and $\Omega e^{-2i\phi j} |\downarrow\rangle\langle 0|$ [see Fig. 1(c)], which would induce a spiral on-site spin-vector and tensor field. To see this, we write down the tight-binding Hamiltonian for such Raman processes $H_\Omega = \sqrt{2}\Omega \sum_j (e^{2i\phi j} \hat{b}_{j\uparrow}^\dagger \hat{b}_{j0} + e^{-2i\phi j} \hat{b}_{j0}^\dagger \hat{b}_{j\downarrow} + \text{H.c.})$, Ω is the Raman coupling strength, $\phi = \pi \cos(\eta) \lambda_L/\lambda_\Omega$ describes the flux and can be tuned by the angle η . In the Mott limit, H_Ω can be treated as spiral spin-vector and spin-tensor Zeeman fields $H_{\text{spin}}^\Omega = 2\Omega \sum_j [\cos(2\phi j) S_j^x - \sin(2\phi j) N_j^{yz}]$, where $N^{\alpha\beta} = \{S^\alpha, S^\beta\}/2 - \delta_{\alpha\beta} \mathbf{S}^2/3$ with $\{\}$ the anticommutation relation and $\alpha(\beta) = (x, y, z)$, Ω is the Zeeman field strength, and ϕ is the spiral period of the field. The total Hamiltonian of our system reads

$$H_{\text{spin}} = H_{\text{spin}}^0 + H_{\text{spin}}^\Omega. \quad (1)$$

The competition between spin interaction H_{spin}^0 and spiral on-site field H_{spin}^Ω may induce many novel spin-tensor magnetic phases, where both spin-vector and spin-tensor have to be considered to fully describe these quantum magnetic orders.

Description of spin-1 magnetic order.— The local magnetic order of a spin-1 system can be described by the local densities of 8 spin-moments (i.e., 3 spin-vectors and 5 spin-tensors). Here we consider the local spin-vector $\vec{S}_j = (\langle S_j^x \rangle, \langle S_j^y \rangle, \langle S_j^z \rangle)^T$ and the spin-tensor fluctuation matrix T_j whose elements are tensor moments $T_j^{\alpha\beta} = \{\langle S_j^\alpha, S_j^\beta \rangle\}/2 - \langle S_j^\alpha \rangle \langle S_j^\beta \rangle$. Geometrically, \vec{S}_j is characterized by an arrow and T_j by an ellipsoid (with principle axis lengths $l_T^n(j)$ ($n = a, b, c$) and orientations $\vec{v}_T^n(j)$ given by the square-roots of the eigenvalues and eigenvectors of $T_j^{\alpha\beta}$ ⁶⁴). To quantitatively char-

acterize and geometrically visualize the magnetic order, we choose 8 independent geometric parameters that could fully describe the spin arrow and ellipsoid: the length l_S and spherical coordinates θ_S , ϕ_S of the arrow, the two axis lengths $l_T^{a,b}$ with the third axis length $l_T^c = \sqrt{2 - (l_S)^2 - (l_T^a)^2 - (l_T^b)^2}$ and orientational Euler angles θ_T , ϕ_T , ϕ_T' of the ellipsoid, as shown in Fig. 2(a).

Beside the local densities, the characterization of long-range correlations of the magnetic order requires spin-vector and spin-tensor correlations. In our Heisenberg model, only the same-spin-moment correlations are relevant because of the same-spin-moment interactions, and correlation function of spin moment \hat{O} over a distance r can be defined as $C(\hat{O}, r) = (1/L) \sum_j [\langle \hat{O}_j \hat{O}_{j+r} \rangle_\nu - \langle \hat{O}_j \rangle_\nu \langle \hat{O}_{j+r} \rangle_\nu]$, with $\langle \cdot \rangle_\nu$ the average value of the ν -fold degenerate ground-states. The correlations can have the same geometrical representation as the local densities. The spin-vector correlation is described by an arrow \vec{S}_r with $S_r^\alpha = C(S^\alpha, r)$ and spin arrow lengths S_r , while the spin-tensor correlation \mathbb{T}_r is described by an ellipsoid with the principle axis lengths l_r^n given by the tensor-correlation matrix $\mathbb{T}_r^{\alpha\beta} = C(N^{\alpha\beta}, r)$.

Spiral spin-tensor magnetism.— The numerical ground-state phase diagram of the Hamiltonian (1) can be obtained through the DMRG calculation^{65,66}, where the length of the spin chain L is up to 96 sites, and we keep the maximum states at 200 and achieve truncation errors of 10^{-8} . The resulting phase diagram for $\phi/\pi = 1/6$ is plotted in the $\theta - \Omega$ plane in Fig. 2(b). There are three different phases: the ferromagnetic spiral tensor phase (FST) for $0.5 \leq \theta/\pi < 1.25$ and the dimer spiral tensor phase (DST) for $1.25 < \theta/\pi \leq 1.5$, both in the small spiral on-site field Ω region, and the paramagnetic tensor phase (PT) for the large Ω . All these phases possess both spiral spin-vector and -tensor densities and can be distinguished by spin correlations: *i*) For the FST phase, there are spin-vector and spin-tensor long-range correlations with nonzero ferromagnetic order $c_F \equiv \langle S_1^z S_{L/2}^z \rangle$; *ii*) For the DST phase, the dimer-vector and dimer-tensor correlations are long-range with nonzero dimer order $c_D \equiv \langle D_1^{S^z} D_{L/2}^{S^z} \rangle$ (see Appendix D); *iii*) For the PT phase, there is no any long-range correlations. For other spiral period ϕ , quantum phase diagrams are similar, except that the phase transitions may occur at different critical points and the period of the spiral modulation varies in the same way as the spiral period ϕ .

First we consider the region $0.5\pi \leq \theta < 1.25\pi$ with the weak Ω (the bottom-left part in the phase diagram), where the spin interactions are still dominant and the ferromagnetic order remains. At $\Omega = 0$, the spin-vector arrow points to certain direction (assumed to be the z axis) that does not change along the chain, and the spin-tensor ellipsoid is a flat disk in the x - y plane [i.e., $l_T^a = 0$, $\theta_T = 0$ (i.e., a axis is parallel to z axis)] (see Appendix B). In the presence of the spiral Zeeman field ($\Omega > 0$),

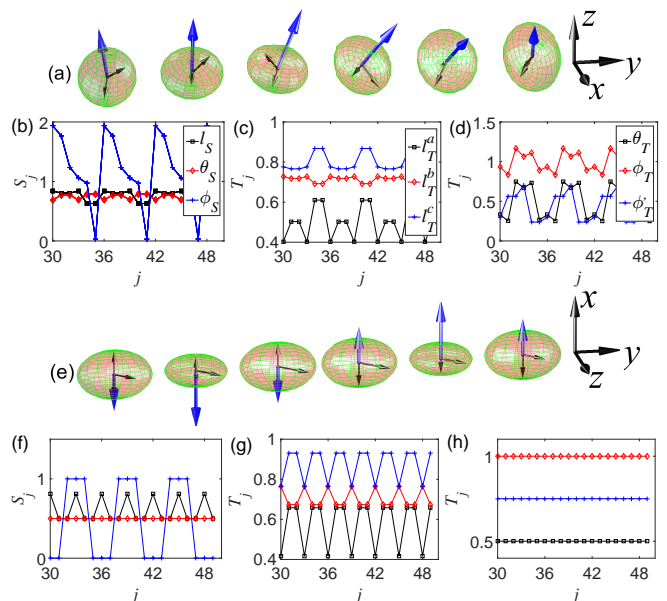


FIG. 3: (a)(e) Schematic diagram of spin-vector density arrows \vec{S}_j and spin-tensor density ellipsoids T_j . (b)(f) Spatial distributions of the spin-vector density arrows \vec{S}_j . (c,d,g,h) Spatial distributions of the spin-tensor density ellipsoids T_j . (a)-(d) FST phase with $\theta/\pi = 0.9$ and $\Omega = 0.4$. (e)-(h) PT phase with $\theta/\pi = 0.9$ and $\Omega = 0.5$. $\phi/\pi = 1/6$ for all subfigures.

the spin-vector density arrows \vec{S}_j , the spin-tensor density ellipsoids T_j , and their relative orientations become oscillating periodically along the chain, forming spiral loops in the Bloch sphere (see Appendix B) and leading to the FST phase, where the local spiral magnetism and long-range correlations coexist. Fig. 3(a) shows the arrows \vec{S}_j and ellipsoids T_j in one spatial period, which possess spiral structure.

For the quantitative characterization of the spiral tensor order, we plot the spatial distributions of $[l_S(j), \theta_S(j), \phi_S(j)]$ for the vector-density arrows, the principle axis lengths $[l_T^a(j), l_T^b(j), l_T^c(j)]$, and the orientational Euler angles $[\theta_T(j), \phi_T(j), \phi_T'(j)]$ of the ellipsoids in Figs. 3(b)-3(d). We find $l_S(j)$, $\theta_S(j)$ and $\phi_S(j)$ oscillate along the chain with the period same as the spiral field, and $\phi_S(j)$ changes from 0 to 2π during one period [see Fig. 3(b)]. Correspondingly, the arrows \vec{S}_j within one period form a circular loop around the z axis (see Appendix B). For the spin-tensor density ellipsoids T_j , beside the modulation in its size $l_T^n(j)$ [see Fig. 3(c)], the corresponding axes form a twisted loop (8-shaped) (see Appendix B), leading to relative rotations between spin-vector density arrows and spin-tensor density ellipsoids $[\theta_T(j), \phi_T(j)$ and $\phi_T'(j)]$ oscillate differently from $\theta_S(j)$, $\phi_S(j)$, as shown in Fig. 3(d). Such spiral magnetic configuration originates from the competition between the on-site spin-vector potential $[\cos(2\phi_j) S_j^x]$ and spin-tensor potential $[-\sin(2\phi_j) N_j^{yz}]$. Without the

spin-tensor field (i.e. only spin-vector field), the spin-vector density arrows and spin-tensor density ellipsoids would rotate similarly with fixed relative orientation [i.e., $\theta_T(j) - \theta_S(j)$, $\phi_T(j) - \phi_S(j)$ and $\phi'_T(j)$ uniform along the chain], and all ellipsoids would have a fixed size [i.e., $l_T^n(j)$ uniform along the chain] (see Appendix C). Moreover, the ferromagnetic spiral order is characterized by the long-range correlation of both spin-vector \vec{S}_r and spin-tensor \mathbb{T}_r (see Appendix B).

As we increase Ω , the spin-vector rotation loop in a period first enlarges and then shrinks to a narrow ellipse (cigar-shaped). For a strong Ω , the system undergoes a second-order phase transition from the FST phase to the PT phase, where the long-range correlations and ferromagnetic order c_F vanish [see Fig. 4(c)]. In the PT phase, the on-site Zeeman field in Hamiltonian (1) dominates, and all spin-vector density arrows are parallel to the Zeeman field [$\cos(2\phi_j) S_j^z$] with length modulations. The corresponding local magnetic densities are shown in Fig. 3(e). Clearly, the spin-vector density loop shrinks into a line on the x -axis in the PT phase ($\theta_S = \pi/2$ and $\phi_S = 0, \pi$).

The rotation loop of the tensor ellipsoids changes similarly as we increase Ω : the loop first enlarges then shrinks into a line after the phase transition, where only the sizes $l_T^n(j)$ (not the direction) of the ellipsoids oscillate (see Appendix B), as shown in Figs. 3(g) and 3(h). The oscillation of $l_T^n(j)$ makes the PT phase different from regular paramagnetic phase. In the PT phase, the vector correlation arrows \vec{S}_r and tensor correlation ellipsoids \mathbb{T}_r decay exponentially (in size) with the distance r , indicating that there does not exist any long-range order (see Appendix B).

Now we turn to the parameter region $1.25 < \theta/\pi \leq 1.5$. The system still stays in the PT phase for a large Ω . For a small Ω , the negative biquadratic interaction dominates, leading to the second-order phase transition to the DST phase. In this phase, the local spin-vector and spin-tensor densities behave similarly as in the PT phase, forming lines instead of spiral loops (see Appendix B). Interestingly, there exist spiral loops for the dimer-vector densities $D_j^{\vec{S}}$ and dimer-tensor densities D_j^T (see Appendix D), thanks to the presence of the on-site spin-tensor field. The ordinary correlations of both spin-vector \vec{S}_r and spin-tensor \mathbb{T}_r decay similarly as the PT phase (see Appendix D). However, there exist long-range correlations for both dimer-vector $\mathbb{D}_r^{\vec{S}}$ and dimer-tensor \mathbb{D}_r^T (see Appendix D), and the dimer order c_D emerges.

Phase transitions.— The phase transitions between above phases can be characterized by the critical behaviors of the local densities and the correlations of the spin-vectors and -tensors. When Ω increases from zero, the spiral loops of spin-vector density arrows \vec{S}_j and spin-tensor density ellipsoids' axes emerge from initial uniform distribution, become larger, then shrink, and finally disappear at the phase transition (see Appendix B). The spin-tensor density ellipsoids T_j have two critical behav-

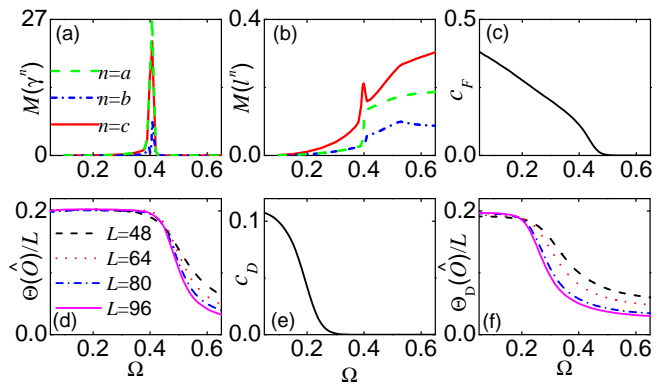


FIG. 4: (a)-(c) Oscillation amplitude of angles $M(\gamma^n)$, lengths $M(l_T^n)$ and ferromagnetic order c_F as a function of Ω . (d) The correlation lengths $\Theta(\hat{O})/L$ as functions of Ω for different lattice length L . (e) Dimer order c_D as a function of Ω . (f) Dimer correlation lengths $\Theta_D(\hat{O})/L$ as functions of Ω for different L , with $\theta/\pi = 1.4$. In (d)(f), we only plot $\hat{O} = S^z$ as an example, others are shown in Supplemental Material (see Appendix E). $\theta/\pi = 0.9$ in (a)-(d), $L = 96$ in (a)-(c) and (e). Common parameter $\phi/\pi = 1/6$.

iors when crossing the phase transition: *i*) the angles $\gamma_j^n = \vec{S}_j \cdot \vec{v}_T^n(j)$ shows a large oscillation in the real space, which can be characterized by a sharp peak for the oscillatory amplitude of angles $M(\gamma_j^n) = \max(\gamma_j^n) - \min(\gamma_j^n)$ located at the phase boundary, as clearly shown in Fig. 4(a); *ii*) the oscillatory amplitude of ellipsoid's axis lengths $M(l_T^n) = \max[l_T^n(j)] - \min[l_T^n(j)]$ have sharp features at the critical point, as shown in Fig. 4(b). In addition, the ferromagnetic order c_F decreases and vanishes across the phase transition, as shown in Fig. 4(c).

The transition from the PT to FST or DST phases corresponds to the formation of the long-range order, therefore the transition should also be captured by more essential correlation lengths. The numerical results for the spin-vector (-tensor) correlation length $\Theta(\hat{O}) = \sqrt{\frac{\sum_{j \neq L/2} (j-L/2)^2 \langle \hat{O}_j \hat{O}_{L/2} \rangle}{2 \sum_{j \neq L/2} \langle \hat{O}_j \hat{O}_{L/2} \rangle}}$ ($\hat{O} = S^{y,z}, T^{yy,zz,xy,xz}$) for the transition between PT and FST phases are shown in Fig. 4(d), which show that there are (no) spin-vector and -tensor long-range correlations for the FST (PT) phase. The critical point Ω_c in the thermodynamic limit is determined by the crossing point between $\Theta(\hat{O})/L$ curves for different finite lattice lengths, as shown in Fig. 4(d).

Similarly, Figs. 4(e) and 4(f) show the dimer order c_D and dimer-vector(-tensor) correlation length $\Theta_D(\hat{O})/L$ for finite lattice lengths, where $\Theta_D(\hat{O}) = \Theta(D_{\hat{O}})$ ($\hat{O} = S^{x,y,z}, T^{xx,yy,zz,xy,xz,yz}$) is used to determine the critical point between PT and DST phases. The dimer correlation length of a finite lattice length retains and then decays. In the decaying region, the dimer correlation lengths of several finite lattices cross at one point. In the process of increasing Ω , the dimer-vector(-tensor) density

spiral loop emerges from a uniform distribution, becomes larger, then shrinks, and finally disappears (see Appendix D).

Discussion and conclusions.— The phase transition is related with the symmetry of the Hamiltonian. For instance, in the FST phase, the ground state is 4-fold degenerate due to spontaneously symmetry breaking of the Z_2 exchange symmetry $S^y \leftrightarrow S^z$ and Z_2 reflection symmetry $S^{y(z)} \leftrightarrow -S^{y(z)}$ of the Hamiltonian (1), leading to nonzero $\langle S^z \rangle$ and $\langle S^y \rangle$. However, in the PT phase, the ground state is non-degenerate, yielding $\langle S^z \rangle = 0$ and $\langle S^y \rangle = 0$, thus the spiral loop shrinks into a line (l_S oscillate, $\theta_S = \pi/2$, $\phi_S = 0, \pi$) [see Fig. 3(f)].

Finally we remark that the local spin states are mixed states for the strongly correlated spin chain, therefore another useful representation of higher-spin pure states, Majorana stars^{27,68–72}, is not suitable for studying correlated quantum magnetism. The spin-tensor can appear not only as an on-site Zeeman field, but also as interactions between nearest-neighbor sites. We show the magnetic order with spin-tensor interaction in Appendix F.

In summary, we propose a new type of quantum magnetism, the spiral spin-tensor order, in a spin-1 Heisenberg chain subject to a spiral spin-tensor Zeeman field. We characterize such quantum spiral spin-tensor orders and their phase transitions using local spin-vector and -tensor densities and their correlations, which can be visualized using eight geometric parameters. To detect such magnetic orders, we can isolate the sites of interest using additional site-resolved potentials and measure their local spin states and non-local spin correlations^{12–15}. Our method can also be used to describe spin-1 quantum magnetism formed by trapped ion array with tunable long-range interactions³³. Our work should lay the foundation for exploring strongly-correlated quantum magnetism in a large spin system and pave the way for engineering novel types of spin-tensor electronic/atomtronic devices.

Acknowledgments

Acknowledgements: X. Z., G. C., and S. J. are supported by National Key R&D Program of China under Grants No. 2017YFA0304203; the NSFC under Grants No. 11674200 and No. 11804204; and 1331KYC. X. L. and C. Z. are supported by AFOSR (FA9550-16-1-0387), ARO (W911NF-17-1-0128), and NSF (PHY-1806227),

Appendix A: Derivation of Hamiltonian (1)

The tight-binding Hamiltonian (1) can be written as three terms

$$H = H_t + H_\Omega + H_U, \quad (\text{A1})$$

where

$$H_t = -t \sum_{\langle i,j \rangle, \sigma} \hat{b}_{i\sigma}^\dagger \hat{b}_{j\sigma}, \quad (\text{A2})$$

$$H_\Omega = 2\Omega \cos(2\phi_j) S_j^x - 2\Omega \sin(2\phi_j) N_j^{yz}, \quad (\text{A3})$$

$$H_U = \frac{U_0}{2} \sum_j \hat{n}_j (\hat{n}_j - 1) + \frac{U_2}{2} \sum_j (\mathbf{S}_j^2 - 2\hat{n}_j). \quad (\text{A4})$$

The effective spin model is obtained through the projection

$$H_{\text{spin}} = P_s H' P_s, \quad (\text{A5})$$

where P_s is the projection operator that projects the states into the low-energy subspace with a filling N (N is an odd integer), H' is the Hamiltonian after the Schrieffer-Wolff transformation⁷³

$$\begin{aligned} H' &= e^{-iO} H e^{iO} \\ &= H - i[O, H] + \frac{1}{2!} [O, [O, H]] + \dots \\ &= H_t + H_U + H_\Omega - i([O, H_t] + [O, H_U] + [O, H_\Omega]) \\ &\quad + \frac{1}{2!} ([O, [O, H_t]] + [O, [O, H_U]] + [O, [O, H_\Omega]]) \\ &\quad + \dots \end{aligned} \quad (\text{A6})$$

In the Mott insulator region, the hopping term H_t is small. We choose O such that $H_t - i[O, H_U] = 0$, thus

$$\begin{aligned} H' &= H_U + H_\Omega - \frac{i}{2} [O, H_t] - i[O, H_\Omega] \\ &\quad + \frac{1}{2!} ([O, [O, H_t]] + [O, [O, H_\Omega]]) + \dots \end{aligned} \quad (\text{A7})$$

Up to the second order of O (H_t is the first order), we have

$$H' = H_U + H_\Omega - \frac{i}{2} [O, H_t] - i[O, H_\Omega] + \frac{1}{2} [O, [O, H_\Omega]]. \quad (\text{A8})$$

Denote P_d as the projection operator that projects the states into the subspace of the high-energy with $N + 1$ filling. Because $H_t = P_s H P_d + P_d H P_s = P_s H_t P_d + P_d H_t P_s$, we have

$$\begin{aligned} O &= P_s O P_d + P_d O P_s \\ &= -i \frac{P_s H_t P_d}{P_d H_U P_d - P_s H_U P_s} + i \frac{P_d H_t P_s}{P_d H_U P_d - P_s H_U P_s}, \end{aligned} \quad (\text{A9})$$

where, $P_d H_U P_d - P_s H_U P_s \approx \langle P_d H_U P_d \rangle - \langle P_s H_U P_s \rangle$. O is not affected by H_Ω . Thus the effective spin Hamiltonian

$$\begin{aligned} H_{\text{spin}} &= P_s H_U P_s + P_s H_\Omega P_s - \frac{i}{2} P_s [O, H_t] P_s \\ &\quad - i P_s [O, H_\Omega] P_s + \frac{1}{2} P_s [O, [O, H_\Omega]] P_s, \end{aligned} \quad (\text{A10})$$

where, $P_s H_U P_s = \text{const}$, $P_s H_\Omega P_s = 2\Omega \cos(2\phi_j) S_j^x - 2\Omega \sin(2\phi_j) N_j^{yz}$,

$$\begin{aligned} -\frac{i}{2} P_s [O, H_t] P_s &= -\frac{1}{2} \frac{P_s H_t P_d H_t P_s}{P_d H_U P_d - P_s H_U P_s} \\ &= \sum_j J_1 \mathbf{S}_j \cdot \mathbf{S}_{j+1} + J_2 (\mathbf{S}_j \cdot \mathbf{S}_{j+1})^2. \end{aligned}$$

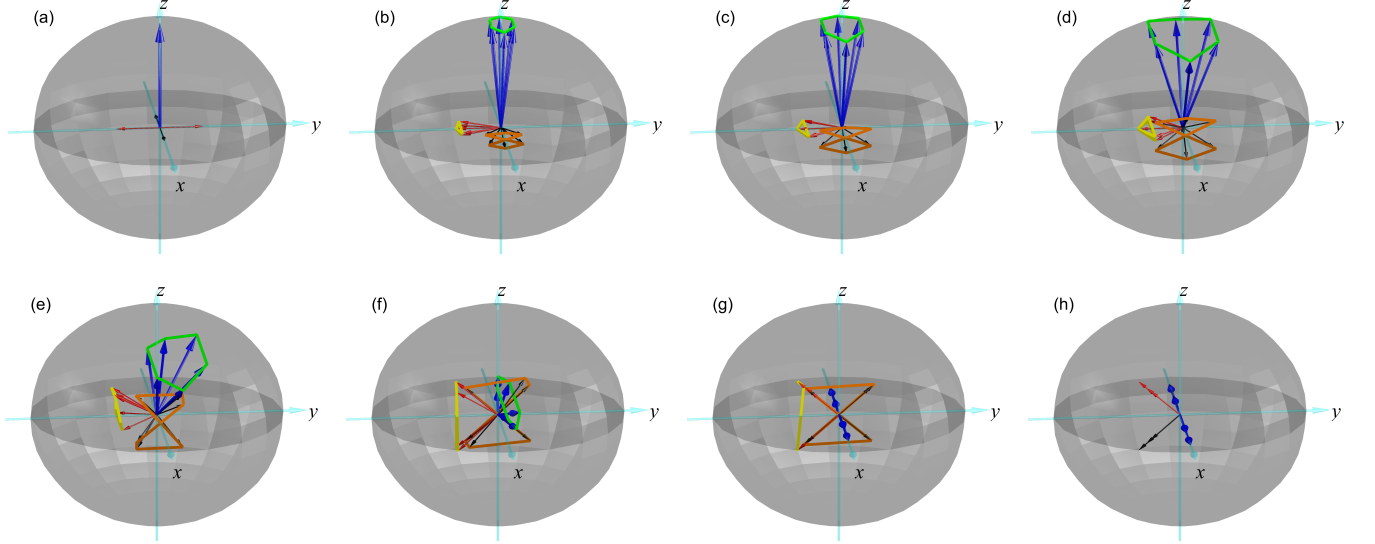


FIG. 5: Spiral loops for the phase transition F-FST-PT. Blue arrows represent spin-vectors, and green line represents the corresponding loop for the spiral loop of the spin-vector density arrows \vec{S}_j^x . Red and black arrows represent two axes of ellipsoids, while yellow and orange lines represent corresponding loops for the spin-tensors density ellipsoids T_j . (a) $\Omega = 0.0$, (b) $\Omega = 0.1$, (c) $\Omega = 0.2$, (d) $\Omega = 0.38$, (e) $\Omega = 0.41$, (f) $\Omega = 0.42$, (g) $\Omega = 0.45$, (h) $\Omega = 0.5$. The phase transition occurs at $\Omega_c = 0.425$. In all subfigures, $\theta/\pi = 0.9$, $\phi/\pi = 1/6$ and $L = 96$.

Here J_1 and J_2 are given by⁷⁴

$$\begin{aligned} -\frac{J_1}{t^2} &= \frac{2(15 + 20n + 8n^2)}{15(U_0 + U_2)} - \frac{16(5 + 2n)n}{75(U_0 + 4U_2)}, \\ -\frac{J_2}{t^2} &= \frac{2(15 + 20n + 8n^2)}{45(U_0 + U_2)} + \frac{4(1 + n)(3 + 2n)}{9(U_0 - 2U_2)} \\ &+ \frac{4n(5 + 2n)}{225(U_0 + 4U_2)}, \end{aligned}$$

$-iP_s[O, H_\Omega]P_s = 0$, and $P_s[O, [O, H_\Omega]]P_s \sim t^2\Omega/U^2 \ll t^2/U$. After ignoring the constant term, the final effective spin Hamiltonian becomes,

$$\begin{aligned} H_{\text{spin}} &= \sum_j J_1 \mathbf{S}_j \cdot \mathbf{S}_{j+1} + J_2 (\mathbf{S}_j \cdot \mathbf{S}_{j+1})^2 \\ &+ 2\Omega \cos(2\phi_j) S_j^x - 2\Omega \sin(2\phi_j) N_j^{yz}. \end{aligned} \quad (\text{A11})$$

Appendix B: Spin-vector and spin-tensor magnetic orders

Without the on-site Zeeman field ($\Omega = 0$), the ferromagnetic spiral tensor (FST) phase reduces to the ordinary ferromagnetic phase (F). The corresponding local magnetic orders represented by the spin-vector density arrows and spin-tensor density ellipsoids' axes are uniform in space, as shown in Fig. 5(a). For the FST with a small Ω , the spin-vector density arrows and spin-tensor density ellipsoids' axes oscillate along the spin chain, forming spiral loops, as shown in Fig. 5(b). With in-

creasing Ω , the spiral loops first enlarge [see Figs. 5(c)-5(d)], then shrink to a narrow ellipse [see Figs. 5(e)-5(g)]. Across the phase transition point to the paramagnetic tensor phase (PT), the loops shrink to lines, where the spin-vector density arrows become parallel to the Zeeman field direction [see Fig. 5(h)].

With increasing Ω , the relative rotation between two neighboring ellipsoids' axes becomes more significant [see Fig. 3(a) in the main text]. In the paramagnetic tensor phase, the relative rotation angle becomes $\pi/2$ [see Fig. 3(e) in the main text]. Both the size and orientation of the ellipsoids oscillate along the spin chain, and a $\pi/2$ orientation change is equivalent to a size deformation without rotation. Therefore in the paramagnetic tensor phase, we only have the modulation in the ellipsoid size [see Fig. 3(e) in the main text].

The ferromagnetic spiral order is characterized by the long-range correlation of both spin-vector \vec{S}_r and spin-tensor \mathbb{T}_r . The spin arrow lengths S_r and axis lengths of ellipsoids l_r^n exhibit power-low decay with the distance r , as shown in Figs. 6(a) and 6(b). In the paramagnetic tensor phase, the vector correlation arrows \vec{S}_r and tensor correlation ellipsoids \mathbb{T}_r decrease (S_r and l_r^n exhibit exponential decay) with the distance r , indicating that there is no long-range order, as shown in Figs. 6(c) and 6(d).

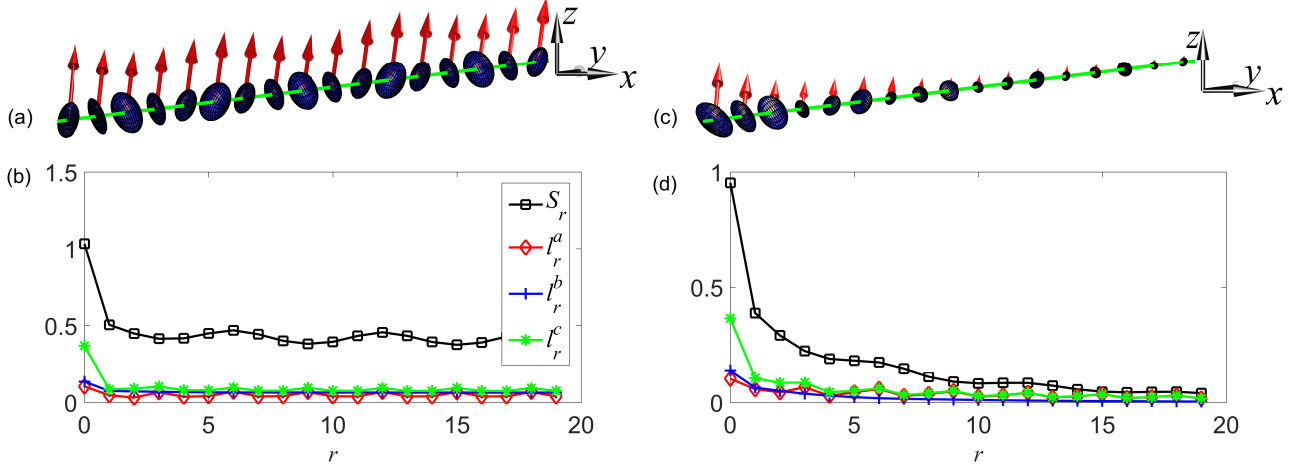


FIG. 6: Spin-vector correlations arrows \vec{S}_r and spin-tensor correlations ellipsoids \mathbb{T}_r ($r = 0, 1, 2, \dots$). (a)(b) FST phase with $\theta/\pi = 0.9$ and $\Omega = 0.4$. (c)(d) Paramagnetic tensor phase with $\theta/\pi = 0.9$ and $\Omega = 0.5$.

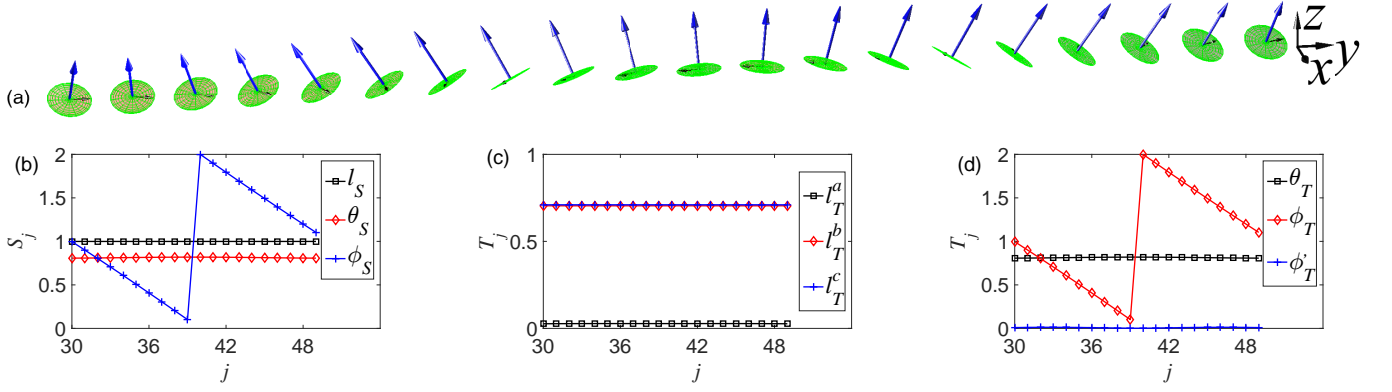


FIG. 7: Ferromagnetic spiral vector phase of Hamiltonian Eq. (14) in Ref. ³⁴ with $\theta/\pi = 1.1$, $\Omega = 0.05$, $\phi/\pi = 1/10$ and $L = 80$. (a) Schematic diagram of spin-vector density arrows \vec{S}_j and spin-tensor density ellipsoids T_j . (b) Spatial distributions of the spin-vector density arrows \vec{S}_j . (c,d) Spatial distributions of the spin-tensor density ellipsoids T_j .

Appendix C: The results due to the spin-vector potential

In contrast, in the ferromagnetic spiral vector phase induced by spiral spin-vector Zeeman field in previous studies³⁴ (tensor results were not discussed in these works), the spin-vector density arrows and spin-tensor density ellipsoids would rotate similarly with fixed relative orientation [i.e. $\theta_T(j) - \theta_S(j)$, $\phi_T(j) - \phi_S(j)$ and $\phi'_T(j)$ are uniform along the chain], and all ellipsoids have fixed sizes [i.e. $l_T^\alpha(j)$ uniform along the chain], as shown in Fig. 7.

Appendix D: Dimer spiral tensor phase

The spin-1 Hamiltonian may support dimer orders in certain parameter region (i.e. $1.25 < \theta/\pi \leq 1.5$), which

describe the pairing order between two neighboring sites. The corresponding dimer-vector and dimer-tensor operators are defined as $D_j^{S^\alpha} = (-1)^j \langle S_{j-1}^\alpha S_j^\alpha - S_j^\alpha S_{j+1}^\alpha \rangle$ and $D_j^{T^{\alpha\beta}} = (-1)^j \langle N_{j-1}^{\alpha\beta} N_j^{\alpha\beta} - N_j^{\alpha\beta} N_{j+1}^{\alpha\beta} \rangle$. For instance, the dimer-vector $D_j^{S^\alpha}$ and dimer-tensor $D_j^{T^{\alpha\beta}}$ are nonzero for the spin singlet pairing between neighboring sites in the dimer phase for the Hamiltonian H_{spin}^0 even without the spiral Zeeman field. Such dimer-vector density $D_j^{\vec{S}}$ and dimer-tensor density D_j^T can also be described geometrically using arrows and ellipsoids, similar as the spin-vector and spin-tensor for a single site. There are also 8 dimer-moments (i.e., 3 dimer-vectors and 5 dimer-tensors): the length l_{DS} and spherical coordinates θ_{DS} , ϕ_{DS} of the arrow, the two axis lengths $l_{DT}^{\alpha,b}$ with the third axis length $l_{DT}^c = \sqrt{2 - (l_{DS})^2 - (l_{DT}^a)^2 - (l_{DT}^b)^2}$ and orientational Euler angles θ_{DT} , ϕ_{DT} , ϕ'_{DT} of the ellipsoid). Similarly, dimer-vector correlation $\mathbb{D}_r^{\vec{S}}$ with

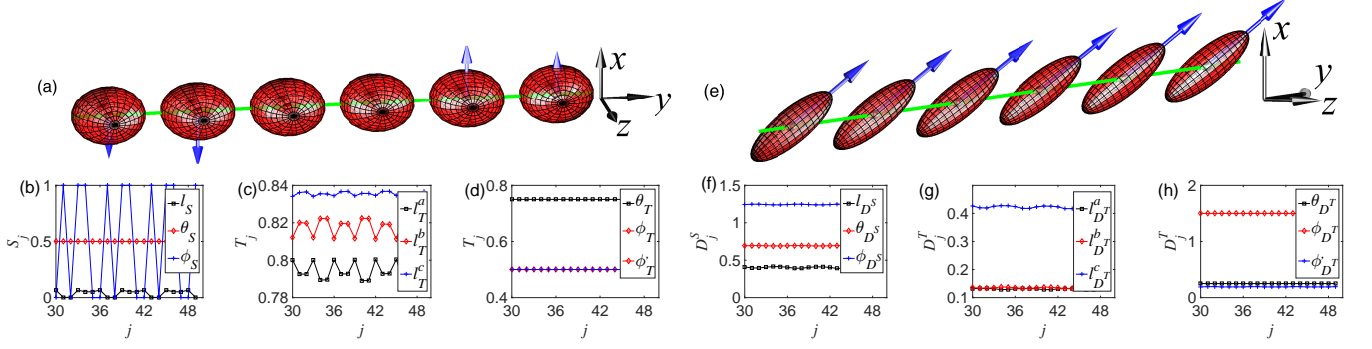


FIG. 8: The orders of the dimer spiral tensor phase. (a) Schematic diagram of spin-vector density arrows \vec{S}_j^s and spin-tensor density ellipsoids T_j^s . (b) Spatial distributions of the spin-vector density arrows \vec{S}_j^s . (c,d) Spatial distributions of the spin-tensor density ellipsoids T_j^s . (e) Schematic diagram of dimer-vector density arrows D_j^s and dimer-tensor density ellipsoids D_j^T . (f) Spatial distributions of the dimer-vector density arrows D_j^s . (g,h) Spatial distributions of the dimer-tensor density ellipsoids D_j^T . In all subfigures, $\theta/\pi = 1.4$, $\Omega = 0.1$, $\phi/\pi = 1/6$, and $L = 96$.

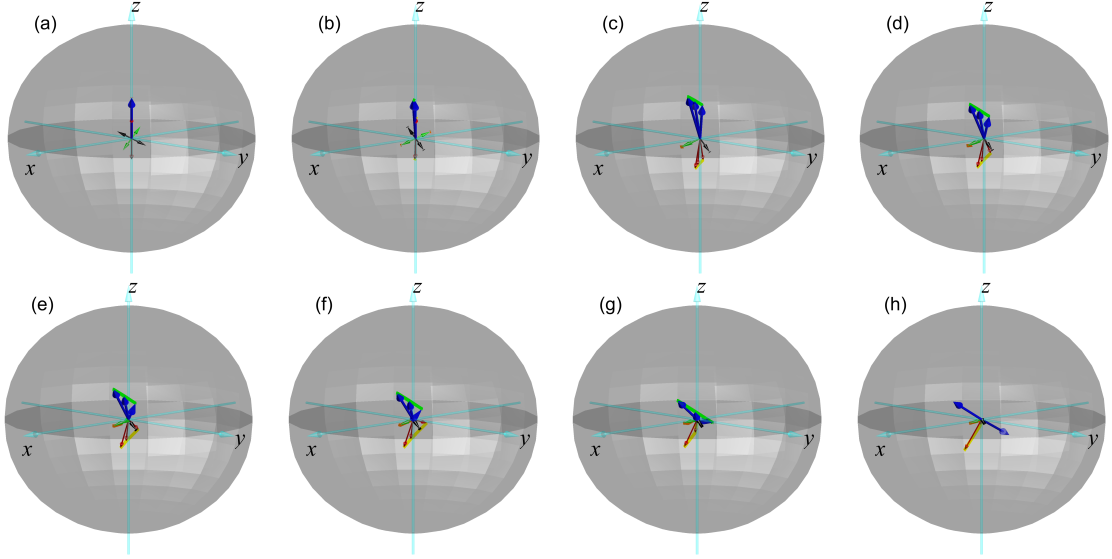


FIG. 9: Phase transition between D-DST-P. Blue arrows represent spin-vectors and green line represents the corresponding loop for the spiral loop of the dimer-vector density arrows D_j^s . Red, green and black arrows represent three axes of ellipsoids, and yellow, orange, and black lines represent corresponding loops for dimer-tensor density ellipsoids D_j^T . (a) $\Omega = 0.0$, (b) $\Omega = 0.1$, (c) $\Omega = 0.18$, (d) $\Omega = 0.2$, (e) $\Omega = 0.21$, (f) $\Omega = 0.22$, (g) $\Omega = 0.25$, (h) $\Omega = 0.3$. The phase transition occurs at $\Omega_c = 0.25$. In all subfigures, $\theta/\pi = 1.4$, $\phi/\pi = 1/6$ and $L = 96$.

elements $\mathbb{D}_r^{S^\alpha} = \mathbb{C}(\mathbb{D}^{S^\alpha}, r)$ can be described by arrows with S_{Dr} the length of arrows, and dimer-tensor correlation \mathbb{D}_r^T can be described by ellipsoids with principle axis lengths l_{Dr}^n ($n = a, b, c$) given by the matrix $\mathbb{D}_r^{T^{\alpha\beta}} = \mathbb{C}(\mathbb{D}^{T^{\alpha\beta}}, r)$, respectively.

The dimer spiral tensor phase (DST) is non-degenerate, therefore the behaviors of spin-vector arrows and spin-tensor ellipsoids are the same as those in the paramagnetic tensor phase [see Fig. 8(a)]. Only the spin-tensor density ellipsoid's lengths $l_T^n(j)$ oscillate, while the angles $\theta_T(j)$, $\phi_T(j)$ and $\phi'_T(j)$ are uniform. Specifically, the size of spin-vector density arrows \vec{S}_j^s and spin-tensor

density ellipsoids T_j^s oscillate along the chain, forming lines in the Bloch sphere that are similar as those for the paramagnetic tensor phase [see Figs. 8(b)-8(d)]. However, the dimer-vector density D_j^s and dimer-tensor density D_j^T can form spiral loops for a finite Ω , as shown in Fig. 8(e). The $l_{Ds}(j)$, $\theta_{Ds}(j)$ and $\phi_{Ds}(j)$ oscillate along the chain [see Fig. 8(f)]. The dimer-tensor ellipsoids' lengths $l_{DT}^n(j)$ and Euler angles $\theta_{DT}(j)$, $\phi_{DT}(j)$, $\phi'_{DT}(j)$ oscillate along the chain [$\theta_{DT}(j)$, $\phi_{DT}(j)$ oscillate differently from $\theta_{Ds}(j)$, $\phi_{Ds}(j)$] [see Figs. 8(g) and 8(h)], originating from different spiral loops for the dimer-vector

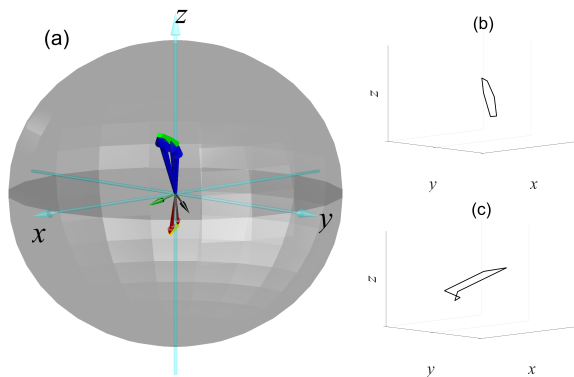


FIG. 10: Spiral loops for the DST with a phase shift $\pi/15$ between vector and tensor terms in the on-site Zeeman field modulation along the chain. (a) Blue arrows represent spin-vectors, and green line represents the corresponding loop for the spiral loop of dimer-vector density arrows $D_j^{\vec{S}}$. Red, green and black arrows represent three axes of ellipsoids, while yellow, orange and black lines represent corresponding loop for the dimer-tensor densities ellipsoids D_j^T . $\Omega = 0.18$, $\theta/\pi = 1.4$, $\phi/\pi = 1/6$ and $L = 96$. (b) The enlarged loop of dimer-vector density arrows. (c) The enlarged loop of one axe (red arrows) of dimer-tensor density ellipsoids.

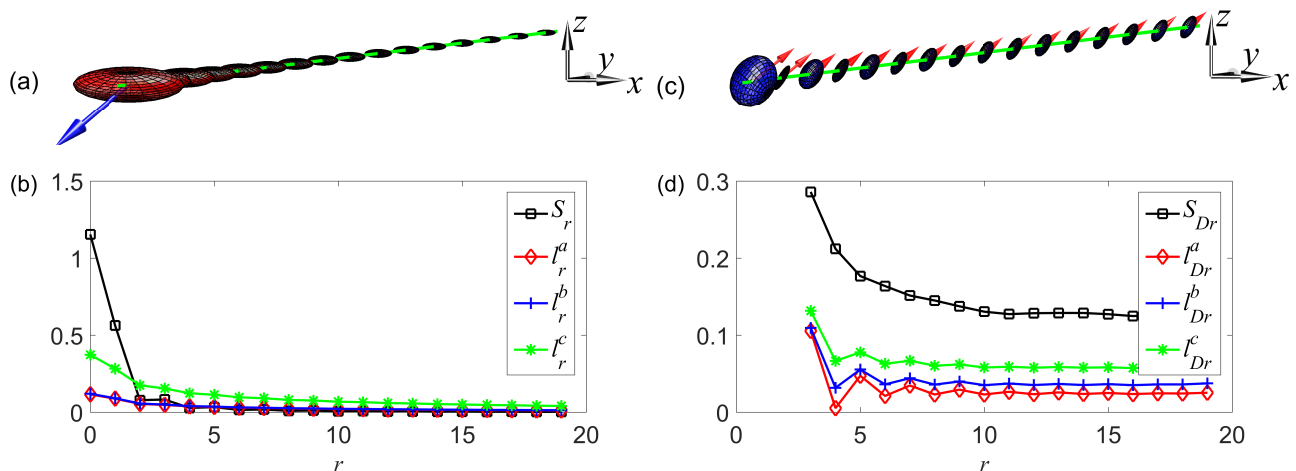


FIG. 11: (a)(b) Spin-vector correlation arrows \vec{S}_r and spin-tensor correlation ellipsoids \mathbb{T}_r . (c)(d) Dimer-vector correlations arrows $\mathbb{D}_r^{\vec{S}}$ and dimer-tensor correlations ellipsoids \mathbb{D}_r^T . In all subfigures, $\theta/\pi = 1.4$, $\Omega = 0.1$, $\phi/\pi = 1/6$, and $L = 96$.

arrows $D_j^{\vec{S}}$ and the dimer-tensor ellipsoid D_j^T .

For the ordinary dimer phase (D) with $\Omega = 0$, the dimer-vector density arrows and dimer-tensor density ellipsoids' axes are uniform in space, as shown in Fig. 9(a). In the dimer spiral tensor phase with increasing Ω , the spiral loop for the dimer order first enlarges [see Figs. 9(b)-9(g)], then shrinks into a point at the phase transition to the paramagnetic tensor phase [see Fig. 9(h)]. For the on-site Zeeman field given in the main text, the system has a mirror symmetry, therefore the spiral loops formed by the dimer densities shrink to lines. If a phase shift between spin-vector and -tensor terms is introduced to the on-site Zeeman field modulation along the chain, the mirror symmetry is broken and the dimer spiral loops would emerge as circles. In addition, the dimer-vector density $D_j^{\vec{S}}$ and dimer-tensor density D_j^T form different spiral loops, leading to relative

rotations between them, as shown in Fig. 10.

There is no long-range ordinary correlations of spin-vector \vec{S}_r and spin-tensor \mathbb{T}_r in the dimer spiral tensor phase [see Figs. 11(a) and 11(b)], which are the same as the paramagnetic tensor phase [see Figs. 6(c) and 6(d)]. Instead, the system possesses long-range dimer correlations for both dimer-vector $\mathbb{D}_r^{\vec{S}}$ and dimer-tensor \mathbb{D}_r^T , the length of arrows S_{Dr} and the axes length of ellipsoids l_{Dr}^n ($n = a, b, c$) exhibit power-low decay and have long-range correlations [see Figs. 11(c) and 11(d)].

Appendix E: Correlation lengths near phase transitions

The critical point Ω_c for the phase transition between ferromagnetic spiral tensor and paramagnetic ten-

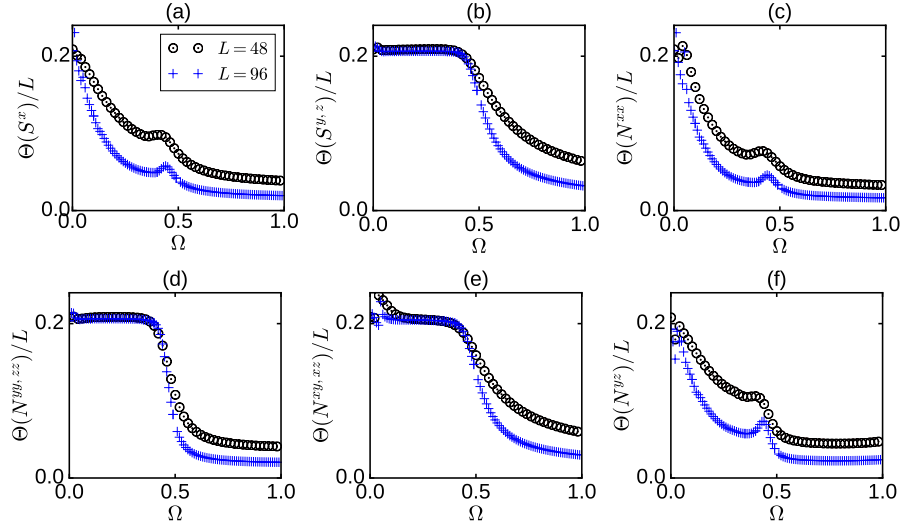


FIG. 12: Spin-vector(-tensor) correlation lengths $\Theta(\hat{O})$ as functions of Ω for different lattice length L across the phase transition between FST and P. In all subfigures, $\theta/\pi = 0.9$ and $\phi/\pi = 1/6$.

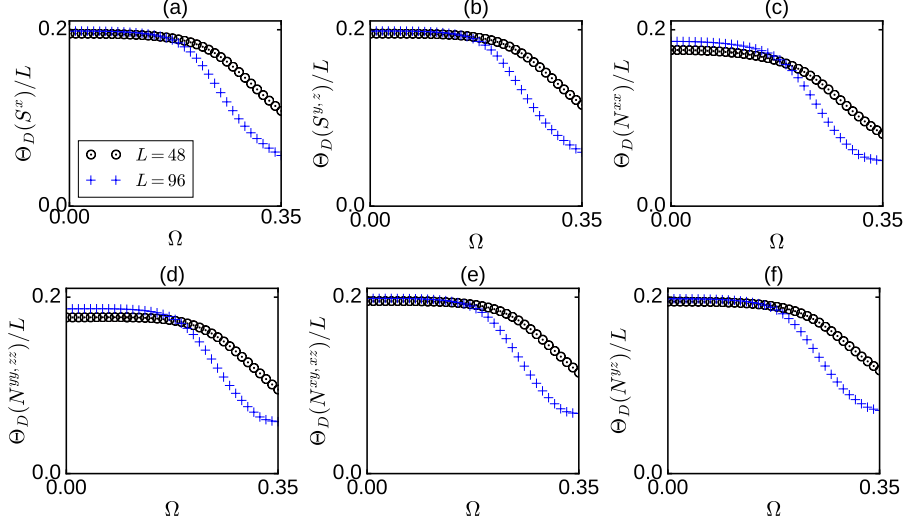


FIG. 13: Dimer-vector(-tensor) correlation lengths $\Theta_D(\hat{O})/L$ as functions of Ω for different lattice length L across the phase transition between DST and P. In all subfigures, $\theta/\pi = 1.4$ and $\phi/\pi = 1/6$.

vector phases in the thermodynamic limit can be examined by the spin-vector(-tensor) correlation lengths $\Theta(\hat{O})$ ($\hat{O} = S^{y,z}, T^{yy,zz,xy,xz}$). The DMRG results show that $\Theta(\hat{O})/L$ for several finite lattice lengths cross at one point with increasing Ω , which is the critical point Ω_c between ferromagnetic spiral tensor and paramagnetic tensor phases, as shown in Fig. 12.

Similarly, the phase transition between dimer spiral tensor and paramagnetic tensor phases in the thermodynamic limit can be examined by the dimer-vector(-tensor) correlation lengths $\Theta_D(\hat{O})/L$ ($\hat{O} = S^{x,y,z}, T^{xx,yy,zz,xy,xz,yz}$). There is (no) long-range dimer correlation in the thermodynamic limit for the dimer spiral tensor (paramagnetic tensor) phase. With increas-

ing Ω , the dimer correlation length $\Theta_D(\hat{O})/L$ for a finite lattice retains and then decays. In the decay region, $\Theta_D(\hat{O})/L$ for several finite lattice lengths cross at one point, which corresponds to the phase transition critical point Ω_c , as shown in Fig. 13.

Appendix F: Magnetic order with spin-tensor interaction

The spin-tensor can appear not only as an on-site Zeeman field, but also as interactions between nearest-neighbor sites. The biquadratic term of Hamiltonian (1) in the main text contains many types of spin-tensor in-

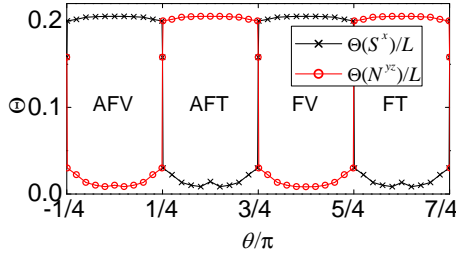


FIG. 14: Phase diagrams, the spin-vector correlation length $\Theta(S^x)/L$, and the spin-tensor correlation length $\Theta(N^{yz})/L$ as functions of θ . The phases are the ferromagnetic vector (FV), antiferromagnetic vector (AFV), ferromagnetic tensor (FT), and antiferromagnetic tensor order (AFT). $\Omega = 0.1$, $\phi/\pi = 1/6$ and $L = 96$.

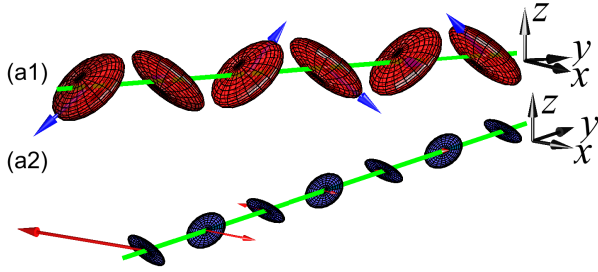


FIG. 15: Spin-vector and -tensor order and correlation in the AFT. (a1) Spin-vector density arrows \vec{S}_j and spin-tensors density ellipsoids T_j . (a2) Spin-vector correlation arrows \vec{S}_r and spin-tensors correlation ellipsoids T_r ($r = 1, 2, \dots$). In all subfigures, $\theta/\pi = 0.3$, $\Omega = 0.1$, $\phi/\pi = 1/6$ and $L = 96$. The arrows are enlarged by 8 times.

interactions, making it hard to identify the spin-tensor correlations induced by each term. Moreover, the spin-

tensor correlations cannot be isolated out because they are bound with the spin-vector correlations. Here we consider a simple toy spin Hamiltonian,

$$H_{\text{spin}} = \sum_j J_a S_j^x S_{j+1}^x + 4J_b N_j^{yz} N_{j+1}^{yz} + 2\Omega \cos(2\phi j) S_j^x - 2\Omega \sin(2\phi j) S_j^y, \quad (\text{F1})$$

where $J_a = \cos \theta$ and $J_b = \sin \theta$. The competition between the spin-vector and spin-tensor interactions induces ferromagnetic or antiferromagnetic vector or tensor phases for different θ , as shown in Fig. 14.

A weak spiral zeeman field (here we take $\Omega = 0.1$) can induce spiral spin-vector densities, but does not affect the long-range magnetic order. We find that the ferromagnetic (antiferromagnetic) vector phases are similar as those discussed in Ref.³⁴, where the system possesses both long-range vector and tensor correlations with spiral spin-vectors densities, and the long-range tensor correlations are induced by the spin-vector interactions. In ferromagnetic (antiferromagnetic) tensor phase [FT (AFT)], the system only possesses long-range spin-tensor correlations (with no long-range spin-vector correlations), which are induced directly by the spin-tensor interactions. In the AFT phase, the spin-tensor density ellipsoids T_j have orthogonal axes $\diagup \diagdown \diagup \diagdown$ between nearest-neighbor sites, while in the FT phase, the axes of the ellipsoids T_j are parallel $\diagdown \diagdown \diagdown \diagdown$ between nearest-neighbor sites. In both the FT and AFT phases, the spin-vector density arrows \vec{S}_j are spiral along the chain. Such FT and AFT phases due to the spin-tensor interactions are very different from previous studies of spin-vector interactions. As examples, in Figs. 15(a1)-15(a2), we show the magnetic local densities and non-local correlations in the AFT phase.

* Electronic address: chengang971@163.com

† Electronic address: chuanwei.zhang@utdallas.edu

¹ A. Auerbach, *Interacting electrons and quantum magnetism* (Springer, New York, 1994).

² U. Schollwöck, J. Richter, D. J. J. Farnell, and R. F. Bisho, *Quantum magnetism* (Springer, New York, 2008).

³ S. Sachdev, *Quantum magnetism and criticality*, *Nat. Phys.* **4**, 173 (2008).

⁴ I. Dzyaloshinskii, A thermodynamic theory of weak ferromagnetism of antiferromagnetics, *J. Phys. Chem. Solids* **4**, 241 (1958).

⁵ T. Moriya, Anisotropic superexchange interaction and weak ferromagnetism, *Phys. Rev.* **120**, 91 (1960).

⁶ E. Manousakis, The spin-1/2 Heisenberg antiferromagnet on a square lattice and its application to the cuprous oxides. *Rev. Mod. Phys.* **63**, 1 (1991).

⁷ F. D. M. Haldane, Nonlinear field theory of large-spin heisenberg antiferromagnets: Semiclassically quantized solitons of the one-dimensional easy-axis néel state, *Phys. Rev. Lett.* **50**, 1153 (1983).

⁸ I. Affleck and F. D. M. Haldane, Critical theory of quantum

spin chains, *Phys. Rev. B* **36**, 5291(1987).

⁹ I. Affleck, T. Kennedy, E. H. Lieb, and H. Tasaki, Rigorous results on valence-bond ground states in antiferromagnets, *Phys. Rev. Lett.* **59**, 799 (1987).

¹⁰ R. Islam, C. Senko, W. C. Campbell, S. Korenblit, J. Smith, A. Lee, E. E. Edwards, C.-C. J. Wang, J. K. Freericks, and C. Monroe, Emergence and frustration of magnetic order with variable-range interactions in a trapped ion quantum simulator, *Science* **340**, 583 (2013).

¹¹ K. D. McAlpine, S. Paganelli, S. Ciuchi, A. Sanpera, and G. D. Chiara, Magnetic phases of spin-1 lattice gases with random interactions, *Phys. Rev. B* **95**, 235128 (2017).

¹² J. Simon, W. S. Bakr, R. Ma, M. E. Tai, P. M. Preiss, and M. Greiner, Quantum simulation of antiferromagnetic spin chains in an optical lattice, *Nature (London)* **472**, 307 (2011).

¹³ M. F. Parsons, A. Mazurenko, C. S. Chiu, G. Ji, D. Greif, and M. Greiner, Site-resolved measurement of the spin-correlation function in the Fermi-Hubbard model, *Science* **353**, 1253 (2016).

¹⁴ A. Mazurenko, C. S. Chiu, G. Ji, M. F. Parsons, M.

- Kanász-Nagy, R. Schmidt, F. Grusdt, E. Demler, D. Greif, and M. Greiner, A cold-atom Fermi-Hubbard antiferromagnet, *Nature (London)* **545**, 462 (2017).
- 15 M. Boll, T. A. Hilker, G. Salomon, A. Omran, J. Nespolo, L. Pollet, I. Bloch, and C. Gross, Spin- and density-resolved microscopy of antiferromagnetic correlations in Fermi-Hubbard chains. *Science* **353**, 1257 (2016).
 - 16 D. Greif, T. Uehlinger, G. Jotzu, L. Tarruell, and T. Esslinger, Short-range quantum magnetism of ultracold fermions in an optical lattice, *Science* **340**, 1307 (2013).
 - 17 R. A. Hart, P. M. Duarte, T.-L. Yang, X. Liu, T. Paiva, E. Khatami, R. T. Scalettar, N. Trivedi, D. A. Huse, and R. G. Hulet, Observation of antiferromagnetic correlations in the Hubbard model with ultracold atoms, *Nature (London)* **519**, 211 (2015).
 - 18 Z. Cai, X. Zhou, and C. Wu, Magnetic phases of bosons with synthetic spin-orbit coupling in optical lattices, *Phys. Rev. A* **85**, 061605 (2012).
 - 19 Z. Cai, H. Hung, L. Wang, and C. Wu, Quantum magnetic properties of the SU(2N) Hubbard model in the square lattice: a quantum Monte Carlo study, *Phys. Rev. B* **88**, 125108 (2013).
 - 20 W. Yang, J. Wu, S. Xu, Z. Wang, and C. Wu, Quantum spin dynamics of the axial antiferromagnetic spin-1/2 XXZ chain in a longitudinal magnetic field, arXiv:1702.01854
 - 21 Z. Wang, J. Wu, W. Yang, A. K. Bera, D. Kamenskyi, A. T. M. N. Islam, S. Xu, J. M. Law, B. Lake, C. Wu, and A. Loidl, Experimental observation of bethe strings, *Nature (London)* **554**, 219 (2018).
 - 22 G. Salomon, J. Koepsell, J. Vijayan, T. A. Hilker, J. Nespolo, L. Pollet, I. Bloch, and C. Gross, Direct observation of incommensurate magnetism in Hubbard chains, *Nature (London)* **565**, 56 (2019).
 - 23 S. R. White and D. A. Huse, Numerical renormalization-group study of low-lying eigenstates of the antiferromagnetic S=1 heisenberg chain, *Phys. Rev. B* **48**, 3844 (1993).
 - 24 J. J. García-Ripoll, M. A. Martin-Delgado, and J. I. Cirac, Implementation of spin Hamiltonians in optical lattices, *Phys. Rev. Lett.* **93**, 250405 (2004)
 - 25 M. Rizzi, D. Rossini, G. De Chiara, S. Montangero, and R. Fazio, Phase diagram of spin-1 bosons on one-dimensional lattices, *Phys. Rev. Lett.* **95**, 240404 (2005).
 - 26 C. D. Hamley, C. S. Gerving, T. M. Hoang, E. M. Bookjans, and M. S. Chapman, Spin-nematic squeezed vacuum in a quantum gas, *Nat. Phys.* **8**, 305 (2012).
 - 27 D. M. Stamper-Kurn and M. Ueda, Spinor Bose gases: Symmetries, magnetism, and quantum dynamics, *Rev. Mod. Phys.* **85**, 1191 (2013).
 - 28 M. Piraud, Z. Cai, I. P. McCulloch, and U. Schollwöck, Quantum magnetism of bosons with synthetic gauge fields in one dimensional optical lattices: A density-matrix renormalizationgroup study, *Phys. Rev. A* **89**, 063618 (2014).
 - 29 S. S. Natu, X. Li, and W. S. Cole, Striped ferromagnetic ground states in a spin-orbit-coupled S=1 Bose gas, *Phys. Rev. A* **91**, 023608 (2015).
 - 30 D. Campbell, R. Price, A. Putra, A. Valdés-Curiel, D. Trypogeorgos, and I. B. Spielman, Magnetic phases of spin-1 spin-orbit-coupled Bose gases, *Nat. Commun.* **7**, 10897 (2016).
 - 31 G. Martone, F. Pepe, P. Facchi, S. Pascazio, and S. Stringari, Tricriticalities and quantum phases in spin-orbit-coupled spin-1 Bose gases, *Phys. Rev. Lett.* **117**, 125301 (2016).
 - 32 E. J. König and J. H. Pixley, Quantum field theory of nematic transitions in spin orbit coupled spin-1 polar bosons, *Phys. Rev. Lett.* **121**, 083402 (2018).
 - 33 C. Senko, P. Richerme, J. Smith, A. Lee, I. Cohen, A. Retzker, and C. Monroe, Realization of a Quantum Integer-Spin Chain with Controllable Interactions, *Phys. Rev. X* **5**, 021026 (2015).
 - 34 J. H. Pixley, W. S. Cole, I. B. Spielman, M. Rizzi, and S. D. Sarma, Strong-coupling phases of the spin-orbit-coupled spin-1 Bose-Hubbard chain: Odd-integer Mott lobes and helical magnetic phases, *Phys. Rev. A* **96**, 043622 (2017).
 - 35 J. Lou, X. Dai, S. Qin, Z. Su, and L. Yu, Heisenberg spin-1 chain in a staggered magnetic field: A density-matrix-renormalization-group study, *Phys. Rev. B* **60**, 52 (1999).
 - 36 J. Lou, C. Chen, J. Zhao, X. Wang, T. Xiang, Z. Su, and L. Yu, Midgap states in antiferromagnetic Heisenberg chains with a staggered field, *Phys. Rev. Lett.* **94**, 217207 (2005).
 - 37 M. Hagiwara, L. P. Regnault, A. Zheludev, A. Stunault, N. Metoki, T. Suzuki, S. Suga, K. Kakurai, Y. Koike, P. Vorderwisch, and J.-H. Chung, Spin excitations in an anisotropic bond-alternating quantum S=1 chain in a magnetic field: Contrast to Haldane spin chains, *Phys. Rev. Lett.* **94**, 177202 (2005).
 - 38 S. R. Manmana, A. M. Läuchli, F. H. L. Essler, and F. Mila, Phase diagram and continuous pair-unbinding transition of the bilinear-biquadratic S=1 Heisenberg chain in a magnetic field, *Phys. Rev. B* **83**, 184433 (2011).
 - 39 G. D. Chiara, M. Lewenstein, and A. Sanpera, Bilinear-biquadratic spin-1 chain undergoing quadratic Zeeman effect, *Phys. Rev. B* **84**, 054451 (2011).
 - 40 K. Rodríguez, A. Argüelles, A. K. Kolezhuk, L. Santos, and T. Vekua, Field-Induced Phase Transitions of Repulsive Spin-1 Bosons in Optical Lattices, *Phys. Rev. Lett.* **106**, 105302 (2011).
 - 41 M. Weyrauch and M. V. Rakov, Dimerization in ultracold spinor gases with Zeeman splitting, *Phys. Rev. B* **96**, 134404 (2017).
 - 42 M. Hermele, V. Gurarie, and A. M. Rey, Mott Insulators of Ultracold Fermionic Alkaline Earth Atoms: Underconstrained Magnetism and Chiral Spin Liquid, *Phys. Rev. Lett.* **103**, 135301 (2009).
 - 43 A. V. Gorshkov, M. Hermele, V. Gurarie, C. Xu, P. S. Julienne, J. Ye, P. Zoller, E. Demler, M. D. Lukin, and A. M. Rey, Two-orbital SU(N) magnetism with ultracold alkaline-earth atoms, *Nat. Phys.* **6**, 289 (2010).
 - 44 S. R. Manmana, K. R. A. Hazzard, G. Chen, A. E. Feiguin, and A. M. Rey, SU(N) magnetism in chains of ultracold alkaline-earth-metal atoms: Mott transitions and quantum correlations, *Phys. Rev. A* **84**, 043601 (2011).
 - 45 B. Yan, S. A. Moses, B. Gadway, J. P. Covey, K. R. A. Hazzard, A. M. Rey, D. S. Jin, and J. Ye, Observation of dipolar spin-exchange interactions with lattice-confined polar molecules, *Nature (London)* **501**, 521 (2013).
 - 46 X. Zhang, M. Bishof, S. L. Bromley, C. V. Kraus, M. S. Safronova, P. Zoller, A. M. Rey, and J. Ye, Spectroscopic observation of SU(N)-symmetric interactions in Sr orbital magnetism. *Science* **345**, 1467 (2014).
 - 47 H. Tsunetsugu and M. Arikawa, Spin nematic phase in S=1 triangular antiferromagnets, *J. Phys. Soc. Jpn.* **75**, 083701 (2006).
 - 48 A. Läuchli, F. Mila, and K. Penc, Quadrupolar phases of the S=1 bilinear-biquadratic Heisenberg model on the triangular lattice, *Phys. Rev. Lett.* **97**, 087205 (2006).
 - 49 S. Bhattacharjee, V. B. Shenoy, and T. Senthil, Possible ferro-spin nematic order in NiGa₂S₄, *Phys. Rev. B* **74**,

- 092406 (2006).
- ⁵⁰ J.-H. Park, S. Onoda, N. Nagaosa, and J. H. Han, Nematic and chiral order for planar spins on a triangular lattice, *Phys. Rev. Lett.* **101**, 167202 (2008)
- ⁵¹ R. K. Kaul, Spin nematic ground state of the triangular lattice $S=1$ biquadratic model, *Phys. Rev. B* **86**, 104411 (2012).
- ⁵² C. Xu, F. Wang, Y. Qi, L. Balents, and M. P. A. Fisher, Spin liquid phases for spin-1 systems on the triangular lattice, *Phys. Rev. Lett.* **108**, 087204 (2012).
- ⁵³ T. A. Tóth, A. M. Läuchli, F. Mila, and K. Penc, Competition between two- and three-sublattice ordering for $S=1$ spins on the square lattice, *Phys. Rev. B* **85**, 140403 (2012)
- ⁵⁴ A. Smerald and N. Shannon, Theory of spin excitations in a quantum spin-nematic state, *Phys. Rev. B* **88**, 184430 (2013).
- ⁵⁵ R. Yu and Q. Si, Antiferroquadrupolar and Ising-Nematic Orders of a Frustrated Bilinear-Biquadratic Heisenberg Model and Implications for the Magnetism of FeSe, *Phys. Rev. Lett.* **115**, 116401 (2015).
- ⁵⁶ J. Dalibard, F. Gerbier, G. Juzeliūnas, and P. Öhberg, Colloquium: Artificial gauge potentials for neutral atoms, *Rev. Mod. Phys.* **83**, 1523 (2011).
- ⁵⁷ N. Goldman, G. Juzeliūnas, P. Öhberg, and I. B. Spielman, Light-induced gauge fields for ultracold atoms, *Rep. Prog. Phys.* **77**, 126401 (2014).
- ⁵⁸ Y.-J. Lin, K. Jiménez-García, and I. B. Spielman, Spin-orbit-coupled Bose-Einstein condensates, *Nature (London)* **471**, 83 (2011).
- ⁵⁹ V. Galitski and I. B. Spielman, Spin-orbit coupling in quantum gases, *Nature (London)* **494**, 49 (2013).
- ⁶⁰ H. Zhai, Degenerate quantum gases with spin-orbit coupling: A review, *Rep. Prog. Phys.* **78**, 026001 (2015).
- ⁶¹ X.-W. Luo, K. Sun, and C. Zhang, Spin-tensor-momentum-coupled Bose-Einstein condensates, *Phys. Rev. Lett.* **119**, 193001 (2017).
- ⁶² D. Li, L. Huang, P. Peng, G. Bian, P. Wang, Z. Meng, L. Chen, and J. Zhang, Experimental realization of a spin-tensor momentum coupling in ultracold Fermi gases, manuscript under review (2020).
- ⁶³ S. K. Yip, Dimer state of spin-1 bosons in an optical lattice, *Phys. Rev. Lett.* **90**, 250402 (2003).
- ⁶⁴ H. M. Bharath, Non-abelian geometric phases carried by the spin fluctuation tensor, *J. Math. Phys.* **59**, 062105 (2018).
- ⁶⁵ S. R. White, Density matrix formulation for quantum renormalization groups, *Phys. Rev. Lett.* **69**, 2863 (1992).
- ⁶⁶ U. Schollwök, The density-matrix renormalization group, *Rev. Mod. Phys.* **77**, 259 (2005).
- ⁶⁷ M. Campostrini, A. Pelissetto, and E. Vicari, Finite-size scaling at quantum transitions, *Phys. Rev. B* **89**, 094516 (2014).
- ⁶⁸ E. Majorana, Atomi orientati in campo magnetico variabile, *Nuovo Cimento* **9**, 43 (1932).
- ⁶⁹ J. H. Hannay, The Berry Phase for Spin in the Majorana Representation, *J. Phys. A* **31**, L53 (1998).
- ⁷⁰ B. Lian, T.-L. Ho, and H. Zhai, Searching for non-Abelian phases in the Bose-Einstein condensate of dysprosium, *Phys. Rev. A* **85**, 051606 (2012).
- ⁷¹ X. Cui, B. Lian, T.-L. Ho, B. L. Lev, and H. Zhai, Synthetic gauge field with highly magnetic lanthanide atoms, *Phys. Rev. A* **88**, 011601 (2013).
- ⁷² H. D. Liu and L. B. Fu, Representation of Berry Phase by the Trajectories of Majorana Stars, *Phys. Rev. Lett.* **113**, 240403 (2014).
- ⁷³ J. R. Schrieffer and P. A. Wolff, Relation between the Anderson and Kondo Hamiltonians, *Phys. Rev.* **149**, 491 (1966).
- ⁷⁴ A. Imambekov, M. Lukin, and E. Demler, Spin-exchange interactions of spin-one bosons in optical lattices: Singlet, nematic, and dimerized phases, *Phys. Rev. A* **68**, 063602 (2003).